Journal Pre-proof

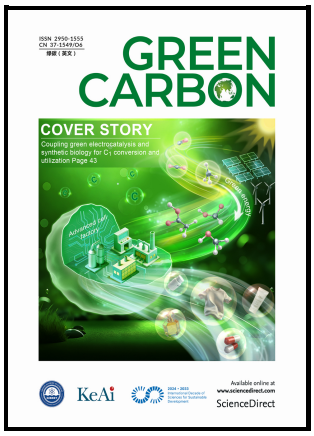

Phosphate-solubilizing bacteria drive transformation and release of phosphorus in phosphorus-enriched sludge biochar: Efficacy validation and multifaceted mechanisms

Sihui Yang, Yifei Wang, Jiayi Yuan, Bing Tian, Xiaolin Xu, Pengfei Cheng, Artem Yurevich Manyakhin, Lina Wei, Jianhua Fan, Xiongfang An

PII: S2950-1555(26)00023-6

DOI: https://doi.org/10.1016/j.greenca.2026.02.004

Reference: GREENC158

To appear in: *Green Carbon*

Received date: 25 November 2025
Revised date: 3 February 2026
Accepted date: 12 February 2026

Please cite this article as: Sihui Yang, Yifei Wang, Jiayi Yuan, Bing Tian, Xiaolin Xu, Pengfei Cheng, Artem Yurevich Manyakhin, Lina Wei, Jianhua Fan and Xiongfang An, Phosphate-solubilizing bacteria drive transformation and release of phosphorus in phosphorus-enriched sludge biochar: Efficacy validation and multifaceted mechanisms, *Green Carbon,* (2026) doi:https://doi.org/10.1016/j.greenca.2026.02.004

Co. Ltd.

Phosphate-solubilizing bacteria drive transformation and release of phosphorus in phosphorus-enriched sludge biochar: Efficacy validation and multifaceted mechanisms

Sihui Yang [a], Yifei Wang [a], Jiayi Yuan [a], Bing Tian [b], Xiaolin Xu [a], Pengfei Cheng [c], Artem Yurevich Manyakhin[d], Lina Wei [e], Jianhua Fan [a,f *], Xiongfang An [a, g *]

[a] School of Chemistry and Chemical Engineering, Shihezi University, Shihezi, 832003, PR China

[b] College of Life Sciences, Zhejiang University, Hangzhou, 310058, PR China

[c] College of Food Science and Engineering, Ningbo University, Ningbo, Zhejiang 315211, PR China

[d] Federal Scientific Center of the East Asia Terrestrial Biodiversity, Far Eastern Branch of the Russian Academy of Sciences, Vladivostok, 690022 Russia

[e] Xinjiang Uygur Autonomous Region Science and Technology Resource Sharing Service Center, 830000, PR China

[f] State Key Laboratory of Bioreactor Engineering, East China University of Science and Technology, Shanghai 200237, PR China

[g] Xinjiang Tianwu Ecological Environmental Protection Co., Ltd., 830000, PR China

* Corresponding author: Jianhua Fan, Tel: 021-64252256, Email address: jhfan@ecust.edu.cn; Xiongfang An, Tel: 0993-2057272, Email address: shz_anxiongf@163.com

Graphic Abstract

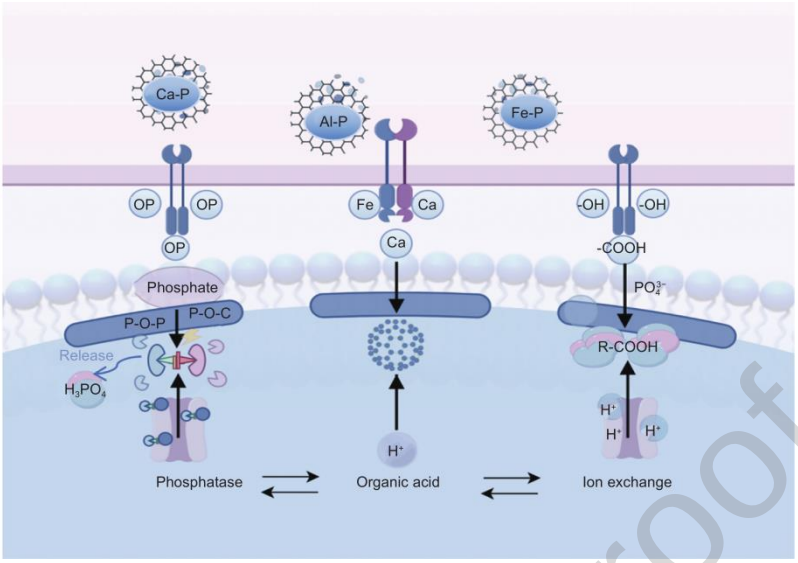

Abstract:

Phosphorus (P) is an essential non-renewable nutrient; however, its inefficient recovery from sewage sludge leads to considerable losses. Although phosphate-solubilizing bacteria (PSB) can convert insoluble P into bioavailable forms, their application is limited by poor colonization and stress tolerance. In this study, a biochar-microbe composite (PSB1@PBC) was prepared by immobilizing PSB *Raoultella ornithinolytica* (PSB1) on P-enriched sludge biochar (PBC) to enhance P transformation and release. PSB1@PBC improved P release and bacterial survival, with cell density 1.51 times that of free-living cells. Hedley sequential extraction showed a decrease in stable HCl-P from 13.20% to 8.90%, whereas bioavailable $NaHCO_3$-P increased by 1.96%. P release followed a biphasic pattern, characterized by an initial rapid phase (0–4 days) followed by a slow and stable phase, peaking at 26.80 mg/g (17.5 times that of unmodified PBC) after 4 days. This improvement is attributed to three synergistic mechanisms: i) microbial acidification via malonic acid secretion, which promotes mineral-bound P dissolution; ii) enzymatic mineralization, which increases phosphatase activity to hydrolyze organic P; and iii) chelation-assisted dissolution through siderophore production. The release of P shifted from slow chemical dissolution in PBC to rapid microbial solubilization in PSB1@PBC, with biochar transport becoming the rate-limiting step. This study demonstrated a sustainable strategy for P recovery, highlighting the potential of PSB1@PBC to enhance nutrient cycling and agricultural sustainability.

Keywords: Phosphorus recovery, Sludge pyrolysis, Phosphate-solubilizing bacteria, Biochar-based microbial agent, Release kinetics

Introduction

Phosphorus (P) is a non-renewable resource that is essential for global ecosystems and agricultural productivity; however, currently the global P reserves are declining[1]. The P content in dried sewage sludge (SS) can reach 3.7%, which is equivalent to 220,000 tons of P, highlighting its importance. Therefore, recovering P from SS to alleviate resource depletion[2]. Although SS incineration can concentrate P in the ash residue and convert it into inorganic phosphates for agricultural use, nutrient loss is common in such treatments[3]. Therefore, alternative environmentally sustainable strategies that enhance SS are urgently required[4]. As a green carbon (C) material, SS-derived biochar offers a promising pathway for P recovery, while concurrently reducing the environmental hazards associated with industrial waste. Sludge pyrolysis, which concentrates P in biochar, has emerged as a promising approach for P recovery. However, over 99% of the P in SS-derived biochar exists in insoluble mineral phases, primarily as calcium phosphate and calcium/magnesium-bound phosphate[5]. This mineral speciation results in extremely low water-soluble P content, which limits its bioavailability[6].

To overcome these limitations and efficiently convert fixed P into plant-available forms in pyrolytic SS biochar, scholars have been proposing biological pathways that are adaptable, sustainable, and effective under complex environmental conditions[7]. Phosphate-solubilizing bacteria (PSB) are a promising solution for solubilizing insoluble P[8]. PSB solubilize P through three main mechanisms: 1) secretion of

organic acids that acidify the microenvironment and facilitate the dissolution of phosphate minerals, 2) production of phosphatases that mineralize organic P, and 3) release of complexing agents that chelate metal cations (e.g., Ca^{2+}, Mg^{2+}, Fe^{3+}, Al^{3+}), thereby promoting the dissociation of insoluble phosphate[9]. Although various P-solubilizing mechanisms have been investigated, the intricate relationships of synergy or antagonism between these mechanisms remain insufficiently elucidated[10]. These processes work synergistically with the acidification of the microenvironment by organic acids, creating an optimal acidic condition that enhances phosphatase activity, whereas metal cation chelation prevents the re-precipitation of the liberated phosphate. Proton efflux via H^+-ATPases sustains local acidity, further promoting mineral dissolution[11]. This integrated system is reinforced by bacterial C metabolism, which provides precursors for organic acid and enzyme biosynthesis. Together, these processes form a coordinated, self-reinforcing solubilization network that maximizes the release of bioavailable P[12].

Despite this potential, free PSB face poor colonization in soil, instability under fluctuating environmental conditions, and high salinity[13]. Recent studies have integrated PSB with biochar to create synergistic microsystems that address these challenges. The porous structure of biochar provides protective niches for microbial colonization, whereas its surface functional groups enhance bacterial adhesion and stabilize extracellular enzymes[14]. This biocompatible interface fosters the formation of robust biofilms through the secretion of extracellular polymeric substances (EPS),

which convert the biochar surface into a bioactive microreactor[15]. Within this microenvironment, adsorbed organic compounds act as metabolic substrates for PSB, promoting the production of organic acids, phosphatases, and electron donors that accelerate mineral phosphate dissolution[16]. Simultaneously, the biochar matrix prevents P re-precipitation by sequestering metal cations. This synergy between PSB and P-enriched sludge biochar (PBC) creates persistent P mobilization hotspots, significantly enhancing P bioavailability through combined microbial and physicochemical mechanisms[17]. Biochar-microbe composites can significantly enhance P availability under environmentally challenging conditions, such as saline–alkaline stress, thereby highlighting their application potential[18,19]. Additionally, advanced characterization has confirmed that biochar acts as a crucial mediator in microbial–mineral interactions, reinforcing the mechanistic foundation of these synergistic systems[20].

Consequently, this study aimed to i) analyze the evolution of P speciation during SS pyrolysis, ii) elucidate the key mechanisms underlying P fixation at high temperatures, iii) screen for efficient, stress-tolerant PSB, and iv) explore their environmental adaptation mechanisms. This investigation was conducted systematically using four integrated experimental modules. The pyrolysis kinetics and P speciation transformation were characterized using thermogravimetric analysis (TGA), X-ray diffraction (XRD), and X-ray photoelectron spectroscopy (XPS) to identify the critical temperature thresholds and the dominant mineral phases

influencing P retention. Subsequently, stress-tolerant PSB strains were isolated through selective cultivation and optimal immobilization parameters were applied to create the PSB1@PBC composite. Additionally, the synergistic mechanisms of P dissolution mediated by organic acid secretion, enzymatic activity, and electron transfer were validated. Finally, the P release kinetics were evaluated to establish a quantitative correlation between P species transformation and bioavailability, providing insights into the bioavailable P pool.

2. Materials and methods

2.1 Preparation of PBC

The SS from the Shihezi Wastewater Treatment Plant (Shihezi XinJiang China) was pretreated to produce biochar. First, the SS was dried at 105 °C to a constant weight and then mechanically crushed and sieved to obtain a homogenized material with a particle size < 2 mm. Biochar was produced by pyrolyzing pretreated SS in a tube furnace under an anaerobic atmosphere created by purging with high-purity N (≥ 99.9%). The temperature was increased to 550 °C at 10 °C/min and maintained for 2 h. Next, the samples were cooled to 25 °C under continuous N flow to yield the PBC.

2.2 Isolation, screening, and identification of *Raoultella ornithinolytica*

PSB were isolated from the SS using a selective medium. SS samples were mixed with a sterile 0.2% NaCl solution (1:100) and incubated at 30 °C and 180 rpm for 16 h. The extracts were serially diluted and plated onto modified NBRIP medium, which

contained: glucose (10.0 g/L, AR grade), $Ca_3(PO_4)_2$ (5.0 g/L, AR grade), $MgCl_2 \cdot 6H_2O$ (5.0 g/L, AR grade), $MgSO_4 \cdot 7H_2O$ (0.25 g/L, AR grade), KCl (0.2 g/L, AR grade), $(NH_4)_2SO_4$(0.1 g/L, AR grade), and agar (15.0 g/L, bacteriological grade).

Colonies forming clear phosphate-solubilization zones were purified using three-zone streaking onto fresh NBRIP plates. The dominant strain was activated in LB medium at 30 °C for 24 h and then in liquid NBRIP medium (1% inoculum) at 30 °C and 180 rpm for 7 days. Soluble P was quantified using the molybdenum-antimony colorimetric method (GB/T 22104-2008).

Molecular identification was performed by extracting genomic DNA using the FastDNA® Spin Kit for Soil. The 16S rRNA gene was amplified using primers 27F and 1492R, and the PCR products were verified using gel electrophoresis. Sanger sequencing was performed, and the sequences were compared to the NCBI database using BLAST. The strain was identified as *R. ornithinolytica*.

2.3 Preparation and growth curve of PSB1@PBC

The PBC samples were pretreated in an autoclave (121 °C, 0.1 MPa) to eliminate endogenous microorganisms. Then, the PBC was mixed with a PSB1 bacterial suspension (logarithmic phase, OD_{600} = 0.8) at a 1:10 mass/volume ratio and incubated at 30 °C and 180 rpm for 2 h to allow bacterial adsorption. For growth curve measurement, 1.0 g of the biochar-bacterial sample was added to 9 mL of sterile

PBS, vortexed for 10 min, and centrifuged at 8,000×g for 5 min. The supernatant containing PSB1@PBC was plated onto LB agar using a gradient dilution method. Plates with 30–300 CFU were incubated at 30 °C for 48 h, and colonies were counted.

2.4 Characterization of SS, PBC, and PSB1@PBC

Scanning electron microscopy (SEM; Hitachi SU8010) at 5.0 kV was used to observe the biochar surface porosity and bacterial distribution. The pyrolysis activation energy was analyzed using the Ozawa method. High-resolution transmission electron microscopy (TEM; JEOL JEM-2100F) was used to examine the bacterial ultrastructure. Thermogravimetric-differential scanning calorimetry (TGA-DSC; NETZSCH STA 449 F5) was used to analyze PBC thermal decomposition up to 550 °C, and activation energy was calculated. XRD (Bruker D8 Advance) revealed hydroxyapatite ($Ca_5(PO_4)_3OH$) and vivianite ($Fe_3(PO_4)_28H_2O$) as the main diffraction peaks. Fourier transform infrared spectroscopy (FTIR; Thermo Nicolet iS50) was used to detect the C-O-P vibration peaks, and XPS (Thermo K-Alpha+) was used to confirm the distribution of carboxyl and phosphate groups on the PBC surface. These analyses provide insights into biochar–microbe interactions.

2.5 Sequential extraction of SS, PBC, and PSB1@PBC

The P forms in PBC and PSB1@PBC were analyzed using Hedley sequential extraction. A 1.00 g sample underwent a four-stage extraction, and each extraction stage was performed with continuous shaking at 180 rpm: 1) Water-soluble P: 100 mL

ultrapure water, extracted for 4 h; 2) $NaHCO_3$-P: 0.5 M buffer solution (pH 8.5±0.1), extracted for 4 h; 3) NaOH-P: 0.1 M alkaline solution (N protection), extracted for 16 h; 4) HCl-P: 1 M acidic solution, extracted for 24 h. Each extract was filtered through a 0.22 μm membrane, and total P (TP) content was determined following HJ 670-2013 standards. Extractions were performed in triplicate.

2.6 Release kinetics of PSB1 and PSB1@PBC

The P solubilization kinetics of PSB1 and PSB1@PBC were studied under controlled conditions. PSB1 was cultured in a modified NBRIP medium containing 10 g/L $Ca_3(PO_4)_2$ and 0.1% (w/v) bromothymol blue (initial pH 7.0). PSB1@PBC (0.5 g) was incubated in 50 mL LB broth under the same conditions. Both cultures were incubated at 30 °C with shaking at 180 rpm. Samples were collected every 24 h for 168 h, centrifuged at 8,000×g for 10 min, and filtered through 0.22 μm membranes. Soluble P (PO_4^{3-}) concentrations were measured using the molybdenum blue method at 700 nm using a UV-2600 spectrophotometer. The P release kinetics were plotted as cumulative P concentration (mg/L) versus time. The dissolution efficiency was calculated as follows:

$$\text{Dissolution}(\%) = \frac{C_{\text{soluble } P}}{C_{\text{total } P \text{ in } Ca_3(PO_4)_2}} \times 100 \qquad (2\text{-}1)$$

where C_{total} P was determined using acid digestion (HNO_3: $HClO_4$ = 4:1, v/v).

To analyze the P release kinetics in PBC and PSB1@PBC, the following five classical kinetic models were employed for data fitting to evaluate the release rate and

underlying mechanisms.

Zero-order Kinetic Model:

$$M_t = k_0 t \quad (2\text{-}2)$$

First-order Kinetic Model:

$$\ln\left(\frac{1}{1-\frac{Mt}{M\infty}}\right) = k_1 t \quad (2\text{-}3)$$

Higuchi Model:

$$M_t = k_2 t^{1/2} \quad (2\text{-}4)$$

Hixson–Crowell Model:

$$\ln\left(\frac{Mt}{M\infty}\right) = k_3 t + k_4 \quad (2\text{-}5)$$

Baker–Lonsdale Model:

$$\left(1-\frac{Mt}{M\infty}\right)^{1/3} = k_5 t \quad (2\text{-}6)$$

where M_t/M_∞ represents the fractional release at different time intervals. Data fitting was performed to calculate the release rate constants (k_0, k_1, k_2, k_3, k_4, k_5) for each model.

2.7 Validation of the dephosphorylation pathway

Bacterial strains were cultured in Pikovskaya medium (0.5% $Ca_3(PO_4)_2$) at 30 °C and 180 rpm for 7 days. After incubation, supernatants were collected using centrifugation (8,000×g, 10 min) and filtered through 0.22 μm membranes. The malonic, glutaric, and butyric acid concentrations were quantified using UPLC-TOF-MS with a mobile phase comprising formic acid, ethyl acetate, and water (5:5:1). To test acid-mediated

solubilization, $Ca_3(PO_4)_2$ or PBC was treated with exogenously added organic acids (malonic, α-ketoglutaric, or butyric acid) at 0.1, 1, 5, and 10 mM. These concentrations were selected to encompass typical physiological levels secreted by PSB. Samples were incubated at 32 °C for 24 h with continuous shaking (180 rpm). After incubation, the suspensions were centrifuged (8,000×g, 10 min) and filtered (0.22 μm). The released soluble P was quantified using the molybdenum blue method and the absorbance was measured at 700 nm. Phosphatase activity was determined by the hydrolysis of p-nitrophenyl phosphate (absorbance at 405 nm). Phytase activity was assessed using sodium phytate hydrolysis. Siderophore production was confirmed using a Chrome Azurol S (CAS) assay and quantified at 465 nm.

2.8 Statistical analysis

Statistical analyses were performed using GraphPad Prism 9.0 (GraphPad Software, USA). Data are presented as the mean ± standard deviation (SD; n = 3). Normality and variance homogeneity were assessed using the Shapiro–Wilk and Levene's tests, respectively. For multiple group comparisons, a one-way ANOVA with Tukey's post hoc test was used. Statistical significance was set at p-value < 0.05.

3. Results and discussion

3.1 Pyrolysis kinetics of P-enriched SS biochar

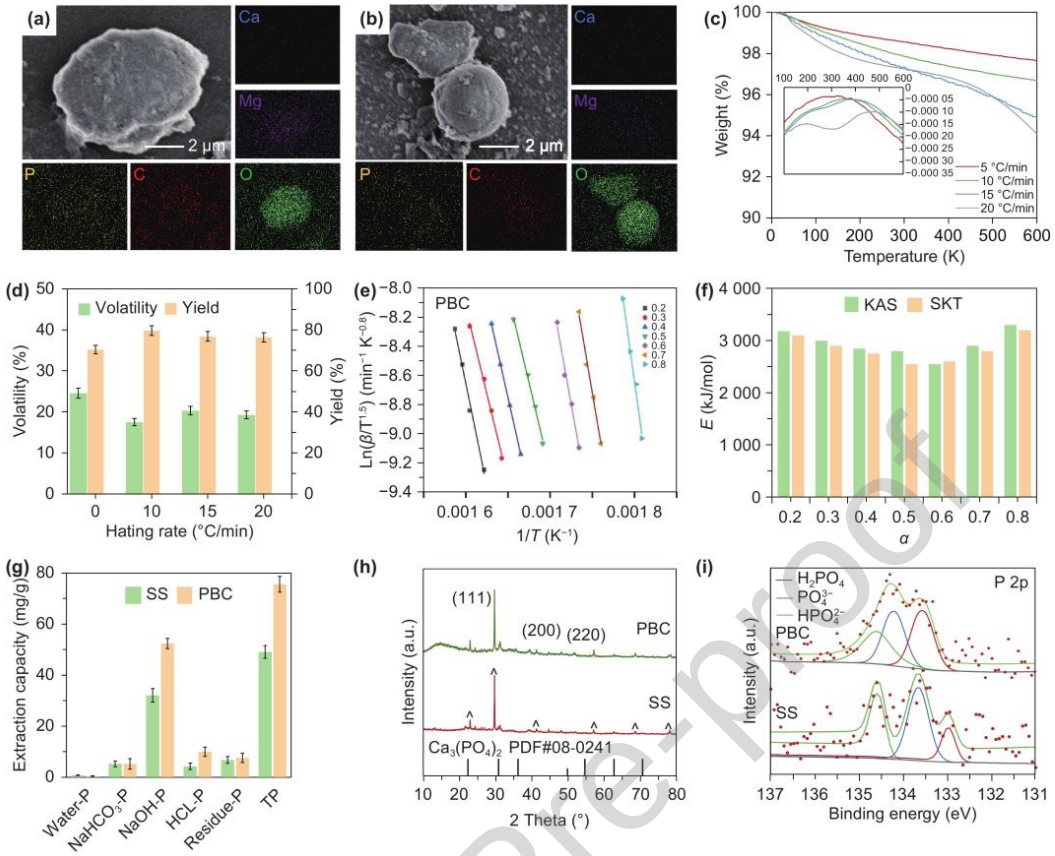

Fig. 1 Characterization and thermal analysis of sewage sludge (SS) and P-enriched sludge biochar (PBC). SEM and elemental mapping of C, O, P, Mg, and Ca for a) SS and b) PBC; c) TGA-DSC curves of SS under different heating rates; d) volatility and yield of PBC under different heating rates; e) linear fitting using the Kissinger–Akahira–Sunose (KAS) method; f) calculated activation energy at different degrees of conversion using the KAS and Starink (SKT) methods; g) P species distribution in SS and PBC; h) XRD patterns of SS and PBC; i) P-XPS spectra of SS and PBC. The data are expressed as the mean ± SD from three independent replicates (n = 3).

Fig. 1a–b shows SEM images highlighting the structural differences between SS and PBC. SS had a rough surface with irregular pores (**Fig. 1a**), whereas PBC formed a well-defined porous network (**Fig. 1b**). This conclusion is supported by the N_2 adsorption–desorption isotherms and pore size distribution profiles (**Fig. S1**). The isotherm curves showed that PBC had a Type IV isotherm with a distinct hysteresis loop at high relative pressures, indicating a well-developed mesoporous structure,

whereas SS exhibited negligible adsorption. In addition, the pore size distribution revealed a prominent peak for PBC at approximately 3.5 nm, whereas SS showed no significant signal. Elemental mapping indicated sparse P distribution in the SS (**Fig. 1a**), but significant colocalization with Ca and Mg in the PBC. The P content was higher in the PBC, suggesting the formation of stable Ca–P and Mg–P phases[21].

Fig. 1c shows TGA-DSC measurements of SS, revealing three pyrolysis stages: moisture evaporation (< 200 °C), organic decomposition (200–500 °C), and inorganic stabilization (> 500 °C). As the heating rate increased from 5°C/min to 20°C/min, the TGA curve steepened, accelerating organic decomposition. **Fig. 1d** shows the comparison between the yield and volatile matter content of PBC produced at heating rates of 5, 10, 15, and 20 °C/min. A heating rate of 10°C/min achieved the highest PBC yield of 79.67% while minimizing volatile loss. This optimal outcome was attributed to the balanced interplay between organic decomposition and the formation of inorganic minerals, particularly Ca/Mg–P, during pyrolysis. In contrast, a heating rate of 5°C/min prolonged the reaction time, leading to excessive C loss. Conversely, heating rates of ≥ 15 °C/min resulted in a rapid volatile release, diminishing the overall PBC yield. Therefore, 10 °C/min was selected as the optimal condition for maximizing P retention and PBC yield[22]. FTIR spectra (**Fig. S2a**) showed reduced O-H, C-H, and C=O peaks in the PBC, indicating the decomposition of the organic components. XPS analysis (**Fig. S2b–c**) confirmed the breakdown of oxygenated groups, supporting the graphitization of organic matter. The SS pyrolysis kinetics

were analyzed using the Kissinger–Akahira–Sunose and Starink methods (**Fig. 1e** and **S2d**). These methods revealed two activation energy regimes. At low conversion ($\alpha < 0.3$), the energy was high due to organic bond cleavage. At higher conversion ($\alpha > 0.7$), activation energy decreased, reflecting mineral-phase reactions dominated by Ca/Mg–P recrystallization (**Fig. 1f**). **Fig. 1g** illustrates the sequential P extraction, showing significant shifts in P speciation. In SS, bioavailable P fractions (Water-P: 0.79 mg/g, $NaHCO_3$-P: 5.25 mg/g) comprised 12.3% of TP, whereas stable mineral-bound phases (HCl-P: 4.27 mg/g, NaOH-P: 32.06 mg/g) dominated 73.90% of TP. In PBC, HCl-P (Ca/Mg-bound) and NaOH-P (Fe/Al-bound) increased to 13.20% and 69.30% of the TP, respectively, reflecting enhanced inorganic stabilization[23]. TP increased from 49.10 mg/g in SS to 75.60 mg/g in PBC, confirming P enrichment during pyrolysis.

Fig. 1h reveals distinct diffraction peaks for calcite ($2\theta = 29.4°$) and hydroxyapatite-like phases ($2\theta = 31.8°$ and 46.7°), corresponding to the (111) and (200) planes of $Ca_3(PO_4)_2$ (JCPDS No. 08-0241) in PBC and SS. These results suggest a crystalline phase evolution in PBC, in contrast to the amorphous nature of SS, indicating inorganic recrystallization and P mineralization during pyrolysis[24]. **Fig. 1i** shows a shift in the P 2p binding energy from 133.5 eV in SS (weakly bound phosphates) to 134.2 eV in PBC, confirming the stabilization of phosphates as $Ca_3(PO_4)_2$ and $Ca_5(PO_4)_3OH$. The XPS analysis of Ca and Mg (**Fig. S2e–f**) further supported this stabilization: the Ca 2p peaks shifted to 347.5 eV, indicating Ca–phosphate bonding,

whereas the Mg 1s spectra narrowed at 1304.2 eV, suggesting Mg–phosphate interactions[25]. These mineral phase transformations, along with the TGA-DSC data, highlight the formation of stable and thermally resilient Ca/Mg–P phases.

3.2 Screening and identification of *R. ornithinolytica*

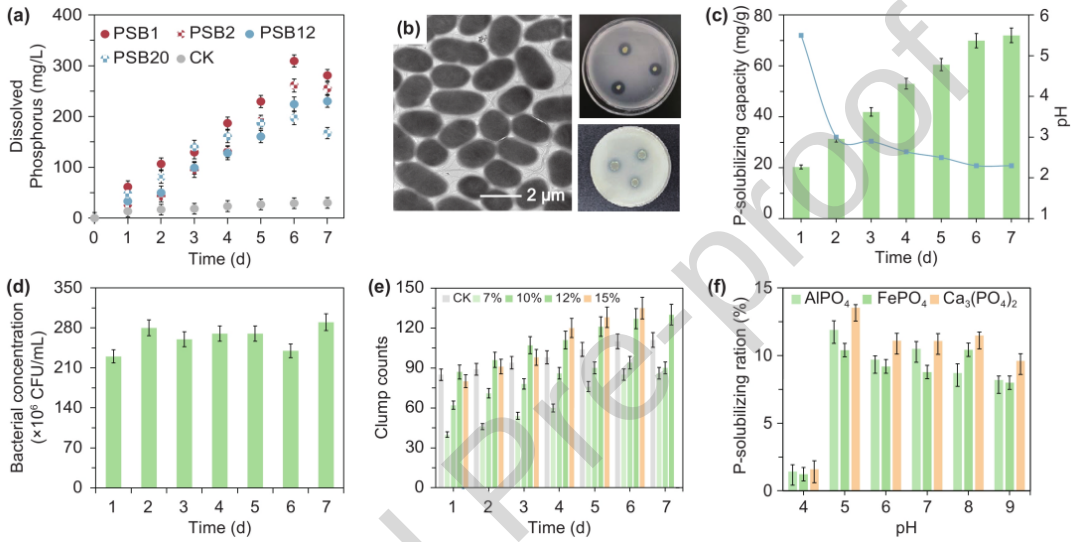

Fig. 2 Phosphorus (P) solubilization and characterization of PSB. a) P dissolution released by PSB strains (PSB1, PSB2, PSB12, PSB20) following cell disruption; b) TEM image and plate of PSB1; c) P-solubilizing kinetics of $Ca_3(PO_4)_2$ by PSB1 and the corresponding pH change dynamics; d) bacterial concentration of PSB1; e) clump counts of $Ca_3(PO_4)_2$ by PSB1 under different saline–alkaline conditions; f) P dissolution rate of PSB1 for insoluble phosphates ($AlPO_4$, $FePO_4$, $Ca_3(PO_4)_2$) under different pH conditions. The data are expressed as the mean ± SD from three independent replicates (n = 3).

Twenty-four morphologically distinct PSB strains were isolated from SS and screened in the NBRIP medium. Initial screening assessed halo formation around the colonies, with D/d ratios ranging from 1.25 to 3.40 after 14 days (**Table S1**), indicating phosphate solubilization. PSB1, PSB2, PSB12, and PSB20 exhibited superior D/d values. The P dissolution content was quantified, with PSB1 showing the highest release (281.04 mg/L), which was 40.50% higher than that of the other strains (**Fig.**

2a). The growth kinetics of PSB1 revealed an S-shaped curve with exponential growth between 6 and 15 h, indicating a critical period for P solubilization (**Fig. S3**). Phylogenetic analysis of the 16S rRNA sequence identified PSB1 as *R. ornithinolytica* with 99.8% similarity to DSM 17521 (**Fig. S4**). TEM imaging confirmed its short rod-shaped morphology (1.5–2.0 μm×0.5–0.8 μm) and smooth surface (**Fig. 2b**). PSB1 demonstrated P solubilization on high-salinity agar (5% NaCl), indicating stress tolerance under osmotically challenging conditions[26].

An inorganic P standard curve was used to study the kinetics of P dissolution and the water-soluble P content of PSB1 was evaluated with respect to pH changes. **Fig. S5** and **S6a** show that the pH decreases sharply from 6.80 to 3.70 within 48 h, then gradually rebounds to 4.10 at 168 h. Water-soluble P increased exponentially from 90 to 112 mg/L in the first 48 h and continued to rise steadily to 241.20 mg/L at 168 h. The initial pH decrease was due to organic acid secretion and enhanced P release, whereas the subsequent pH rebound was attributed to the phosphate buffering system[27]. Despite the rebound in pH, P dissolution continued, indicating sustained microbial activity and acid production. **Fig. 2c** shows that the pH in the insoluble P system decreases from 5.50 to 3.0 within 48 h and remains low between 2.0 and 3.0 until 168 h. The solubilizing capacity increased significantly from 24 to 48 h, reaching 72.01 mg/g at 168 h. The sustained low pH indicated that PSB1 produced sufficient organic acids to exceed the buffering capacity of the system, maintaining a persistently acidic environment. Dynamic pH changes in both systems were strongly

negatively correlated between pH decrease and P-solubilizing capacity in the initial acidic phase (pH < 4.0), supporting acid-promoted P solubilization[28]. After the initial drop, the pH rebounded in the water-soluble-P system but remained low in the insoluble-P system, reflecting differences in buffering capacity and proton flux (**Fig. S6b**). Maximum solubilization was achieved at 168 h in both systems, suggesting efficient P solubilization under buffered and acidic conditions[8]. Survival assays confirmed that PSB1 remained robust, with 98% viability and a cell density of 290×10^6 CFU/mL (**Fig. 2d**).

The solubilization efficiency of insoluble phosphates by PSB1 is influenced by the interplay between salinity, pH, and environmental factors. As shown in **Fig. 2e**, saline–alkaline conditions have a dual effect on $Ca_3(PO_4)_2$ dissolution: low salinity (7% NaCl) suppresses bacterial growth by 22.50%, reducing dissolution due to impaired acid secretion; however, higher salinity (10–15% NaCl) enhanced bacterial growth by 26.12%; this could be attributed to adaptive mechanisms, such as compatible solute biosynthesis and membrane lipid remodeling that help PSB1 maintain metabolic activity under ionic stress. **Fig. 2f** shows the PSB1 P solubilization capacity for the three insoluble phosphates ($AlPO_4$, $FePO_4$, and $Ca_3(PO_4)_2$) at different pH levels. At pH 4.0, solubilization was low because of reduced acid secretion and changes in metal-phosphate speciation. At pH 5.0, solubilization peaked: $Ca_3(PO_4)_2$, $FePO_4$, and $AlPO_4$ reached 72.01 ± 3.20, 55.31 ± 2.30, and 63.28 ± 2.80 mg/g, respectively. This increase was driven by H+-mediated lattice disruption and the

organic acid chelation of metal cations (Ca^{2+}, Al^{3+}, and Fe^{3+}). Notably, $Ca_3(PO_4)_2$ showed a high solubilization rate (≥ 11%) across pH 5.0–9.0 because of weak Ca^{2+} hydrolysis and sustained ligand-promoted dissolution. In contrast, $AlPO_4$ and $FePO_4$ exhibited reduced solubilization above pH 5.0, as the hydrolysis of Al^{3+}/Fe^{3+} formed surface-occluding hydroxides. The PSB1 performance with $Ca_3(PO_4)_2$ aligns with those reported in previous studies showing the efficacy of organic acids in solubilizing Ca phosphates[28]. Additionally, PSB1 maintained high P solubilization across pH 5.0–9.0, surpassing typical results for tricalcium phosphate in alkaline conditions, suggesting enhanced ligand stability or reduced pH sensitivity. The lower solubilization of Al/Fe–P above pH 5.0 reflects the common constraints observed in other PSB strains, where cation hydrolysis governs dissolution kinetics. This highlights the importance of mineralogy and cation-specific interactions for PSB functionality[8,29].

Multifactorial assays showed that PSB1 exhibited a strong tolerance to environmental stress during P solubilization (**Fig. S7**). $Ca_3(PO_4)_2$ solubilization At 37 °C increased by 17.69% compared to that at 27 °C, whereas $AlPO_4$ and $FePO_4$ solubilization improved by 12.81% and 4.23%, respectively, indicating thermal adaptation for proton-driven Ca–P mobilization. At a 1% inoculum concentration, microbial metabolite secretion was insufficient, resulting in the low solubility of all phosphates. Increasing the inoculum to 2% enhanced the cell density and metabolite accumulation, reaching peak P solubility rates of 12.54% for $Ca_3(PO_4)_2$, 11.40% for

$AlPO_4$, and 10.90% for $FePO_4$. Further increases (3–5%) showed only slight improvement, likely due to $AlPO_4$ and $FePO_4$ hydrolysis forming colloidal particles that encapsulate the minerals. $Ca_3(PO_4)_2$ maintained a high solubilization rate owing to its loose crystalline structure.

3.3 Preparation and P solubilization performance of PSB1@PBC

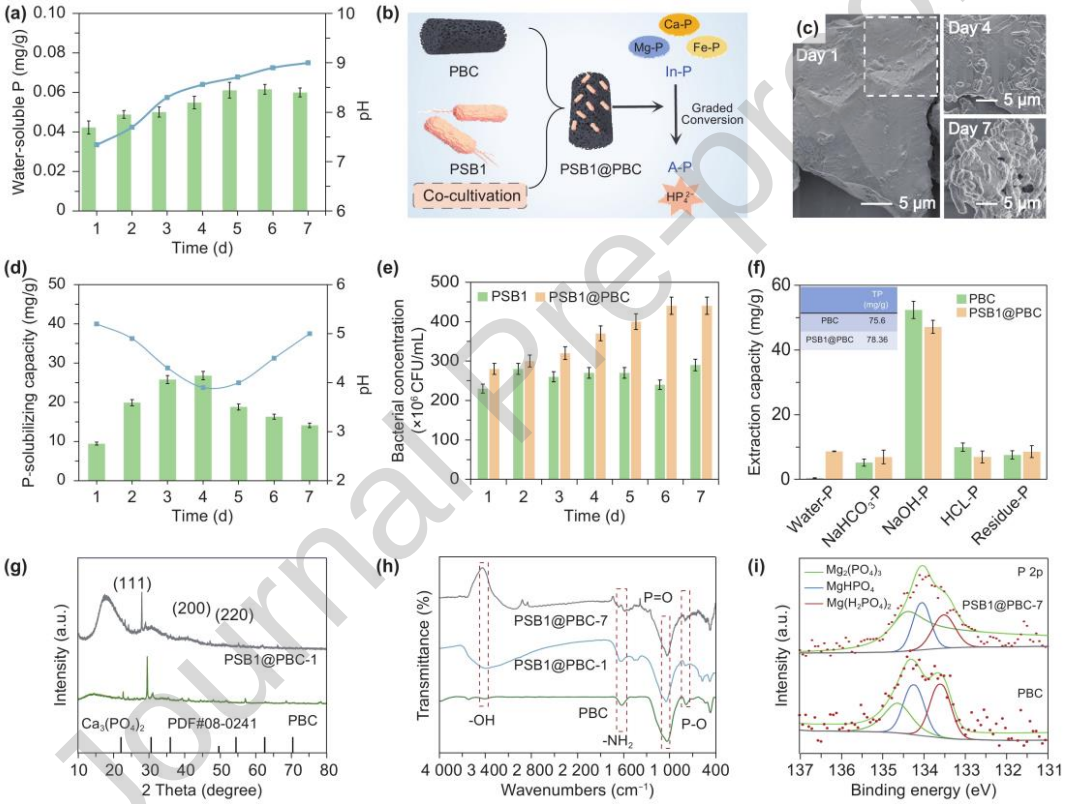

Fig. 3: Characterization and performance of PSB1@PBC. a) Water-soluble P of PBC and the corresponding pH change dynamics; b) process flow diagram for the preparation of a biochar-based bacterial agent (PSB1@PBC) with PSB1 immobilized on PBC; c) SEM images of bacterial dissolution states at 1, 4, and 7 days; d) P solubilization capacity of PSB1@PBC and the corresponding pH change dynamics; e) bacterial concentrations of free PSB1 and immobilized PSB1@PBC; f) P species distribution in PBC and PSB1@PBC analyzed using sequential extraction; g) XRD patterns of PBC and PSB1@PBC-1 (P release after 1 day); h) FTIR spectra of PBC, PSB1@PBC-1, and PSB1@PBC-7 (P release after 7 days); i) XPS analysis of P in PBC and PSB1@PBC-7. The data are expressed as the mean ± SD from three independent replicates (n = 3).

The PBC exhibited low water-soluble P release (0.058 ± 0.012 mg/g) over 7 days, representing only 0.56% of TP. The pH remained near neutral (7.5 ± 1.5, **Fig. 3a**), indicating that P in the PBC was primarily stabilized as Ca/Mg-bound phosphates, rather than being directly bioavailable[30]. This low bioavailability highlights the need for microbial intervention to release fixed P. To address P scarcity and immobilization in SS, PSB1@PBC was developed by immobilizing PSB1 on PBC (**Fig. 3b**). The preparation was incubating PSB1 with sterilized PBC under optimized conditions to enhance microbial attachment and activity. The P forms in PBC that are difficult to utilize can be converted into bioavailable P by immobilized PSB1. The optimal bacteria-to-biochar ratio was 1:5, at which the phosphate dissolution efficiency peaked (**Fig. S8**). **Fig. 3c** shows SEM images of PSB1@PBC immobilization. Initially, PSB1 cells adhered sparsely as isolated rods with increased attachment at the pore edges. After 4 days, the cell density increased, forming microcolonies within the pores. By day 7, dense biofilms had enveloped the surface and formed a continuous microbial layer. This colonization process confirmed that the P-retention capacity of PBC created a stable environment that supports microbial growth and enhances mineral-phosphate reactions.

XPS analysis (**Fig. S9a–b**) showed increased C-O and carboxylate peak intensities in the loaded PBC, indicating a higher surface O content. This functionalization could be attributed to bacterial EPS that provided attachment sites via hydrogen bonding and

electrostatic interactions, driving the morphological changes observed in the SEM images. PSB1@PBC exhibited significantly enhanced P dissolution kinetics compared to free PSB1. Over 7 days, the composite system released soluble P in a biphasic pattern, reaching a maximum P-solubilizing capacity of 26.80 ± 3.10 mg/g by day 4 (**Fig. 3d**). The pH curve showed a sharp decline from 6.0 to 4.8 within 48 h, followed by stabilization driven by organic acid secretion during bacterial growth, which protonated the Ca/Mg phosphate surfaces, disrupted metal-phosphate bonds, and promoted P dissolution[31]. Moreover, under identical NBRIP conditions, PSB1@PBC exhibited superior performance compared with free PSB1 in terms of cumulative P release and sustained dissolution activity. This underscores the synergistic role of biochar in enhancing microbial activity and regulating P release dynamics (**Fig. S10)**. PSB1@PBC reached a bacterial density of 4.40×10^8 CFU/g, 1.51 times that of free cells (2.90×10^8 CFU/mL, **Fig. 3e**). This increase was due to the protective microenvironment provided by the PBC matrix, which shielded bacteria from osmotic pressure and adsorbed growth factors, thereby promoting microbial adhesion[32].

Sequential extraction was performed on PBC and PSB1@PBC (**Fig. 3f**) to clarify the changes in the P forms. Compared with PBC, HCl-P (Ca/Mg-bound P) decreased from 13.20% to 8.90% in PSB1@PBC, whereas $NaHCO_3$-P (available P) increased by 1.96%, from 5.22 to 6.95 mg/g. This change was attributed to bacterial secretions chelating Ca^{2+}/Mg^{2+}, disrupting the $Ca_3(PO_4)_2$ lattice structure, and releasing

bioavailable P[33]. The TP content remained stable (75.60–78.36 mg/g), indicating conversion rather than loss of P. The increase in $NaHCO_3$-P highlighted the enhanced bioavailability, with insoluble P being transformed into soluble forms. XRD analysis showed sharp diffraction peaks for $Ca_3(PO_4)_2$ at 2θ = 31.8° in PBC (**Fig. 3g**), whereas PSB1@PBC exhibited broadened, weakened peaks, suggesting partial dissolution and amorphization[34]. Diffuse signals between 20–25° indicated microbial-induced mineral weathering, where bacterial acidification disrupted the Ca/Mg–P lattice structures and facilitated P release. In the FTIR spectrum (**Fig. 3h**), PSB1@PBC showed enhanced P-related vibration peaks for P=O (1200–1300 cm^{-1}) and P-O (900–1200 cm^{-1}). The P-XPS peak-fitting results (**Fig. 3i**) revealed that bacterial loading increased the number of P functional groups on the PBC surface, promoting the conversion and adsorption of P forms[35]. XPS showed shifts in Ca 2p (from 347.5 eV to 346.9 eV) and Mg 2s (from 1304.2 eV to 1303.6 eV), indicating that bacterial secretions formed carboxylate complexes with Ca^{2+} and Mg^{2+} (**Fig. S9c–d**), suggesting that Mg and Ca participated in chemical reactions on the PBC surface, creating a metal-organic/inorganic composite environment with P-related groups[36].

3.4 Verification of the three main P solubilization pathways by PSB1

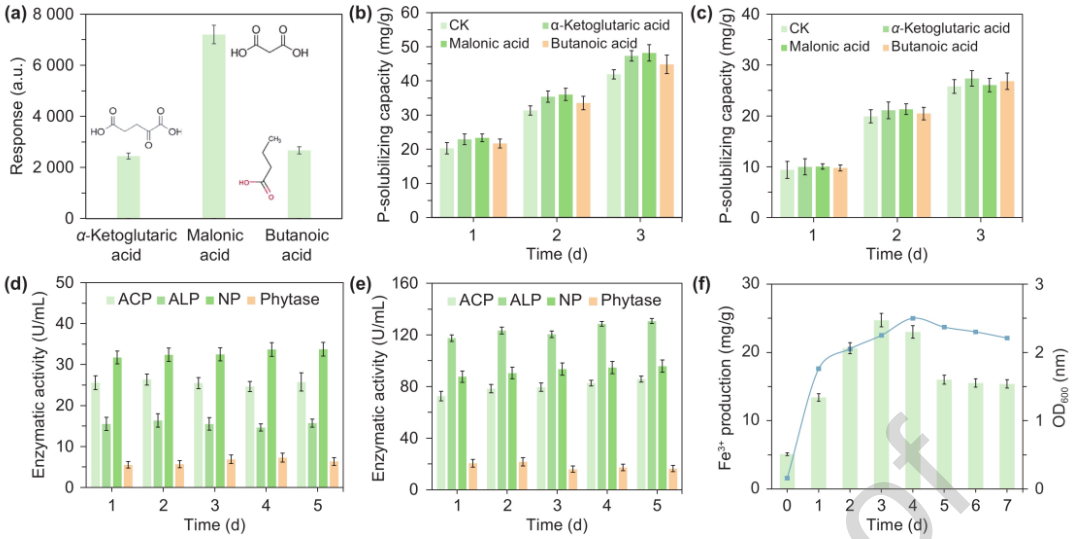

Fig. 4: Role of organic acids, enzymes, and siderophores in P solubilization. a) Response dynamics over 3 days for the three main P-solubilizing organic acids (α-ketoglutaric, malonic, and butyric acids); b) effect of the acids on P solubilization from $Ca_3(PO_4)_2$; c) effect of the acids on P solubilization from PBC; d) enzymatic activity during P solubilization by PSB1 with $Ca_3(PO_4)_2$; e) enzymatic activity during P solubilization by PSB1 with PBC; f) Fe^{3+} production and the corresponding OD_{600} change dynamics. The data are expressed as the mean ± SD from three independent replicates (n = 3).

Fig. 4a shows that PSB1 secreted malonic, α-ketoglutaric, and butyric acids during the critical P solubilization phase (72 h). Malonic acid was the predominant acid (7203 ± 32.04 a.u.), significantly surpassing α-ketoglutaric (2448 ± 41.30 a.u.) and butyric acid (2670 ± 34.01 a.u.). This secretion pattern is attributed to the upregulation of genes encoding malonyl-CoA synthetase (matB) and acetyl-CoA carboxylase (accD) during the stationary phase. The low pKa of malonic acid (2.83) aids in maintaining an acidic microenvironment, which is essential for mineral dissolution. To verify solubilizing capacity, acids were added exogenously to media containing different P sources ($Ca_3(PO_4)_2$ and PBC). **Fig. 4b** shows that all acids enhance P release compared to the uninoculated control in the $Ca_3(PO_4)_2$ system, with malonic acid achieving the highest solubilization (48.19 ± 5.58 mg/g at 72 h). Butyric acid had

delayed efficacy (44.83 ± 2.7 mg/g at 72 h), whereas α-ketoglutaric acid showed rapid initial dissolution (22.93 ± 3.0 mg/g at 24 h). The superior performance of malonic acid is attributed to its bidentate chelation of Ca^{2+} ions, which disrupts the $Ca_3(PO_4)_2$ lattice, the slower kinetics of butyric acid suggest weaker or slower chelation, and the early advantage of α-ketoglutaric acid is likely because of rapid proton release or co-metabolic effects. **Fig. 4c** illustrates the dissolution kinetics of PBC. The solubilization efficiency of exogenous acids was significantly lower than that of $Ca_3(PO_4)_2$. Malonic acid reached only 26.06 ± 2.7 mg/g at 72 h, 45% lower than with $Ca_3(PO_4)_2$. This reduced efficiency is due to the encapsulated $Ca_5(PO_4)_3OH$ in the PBC matrix and microporous diffusion barriers, which limit the acid-mineral contact and extend the dissolution kinetics[37].

Fig. S11a presents a standard curve for quantifying the phosphatase activity, showing that the release of p-nitrophenol from the PNPP substrate follows linear kinetics ($y = 0.002x–0.0118$, $R^2 = 0.9924$). **Fig. S11b** identifies 37 °C as the optimal temperature for phosphatase activity (31.75 ± 3.10 U/mL), significantly higher than that under 30 °C (16.80 ± 1.8 U/mL) and 40 °C (12.50 ± 1.2 U/mL). This temperature dependence reflects enzyme stability and secretion kinetics, with reduced activity at suboptimal temperatures due to decreased catalytic efficiency (30 °C) or enzyme denaturation (40 °C)[17]. **Fig. 4d** shows the dynamic changes in acid phosphatase (ACP), alkaline phosphatase (ALP), nucleases (NP), and phytase during $Ca_3(PO_4)_2$ dissolution by PSB1. ACP activity peaked rapidly at 26.34 U/mL (32.60% of the total

activity) after 48 h, strongly correlating with the soluble P release. ALP activity was lower, peaking at 16.35 U/mL, whereas NP and phytase activities peaked later, with phytase reaching 33.75 U/mL at 168 h. ACP dominance is linked to Ser129 residue stability under acidic conditions, facilitating a strong nucleophilic attack on Ca–P bonds. The inhibition of ALP is due to Zn^{2+}-coordinated site denaturation at low pH, and NP and phytase activities are limited by substrate availability, such as the late accumulation of nucleic acids and scarcity of phytate[38]. **Fig. 4e** shows phosphatase activity in the PBC system. All four phosphatases increased in activity, with ALP being dominant, reaching 123.35 ± 2.90 U/mL at 48 h (86.74% higher than in the $Ca_3(PO_4)_2$ system). ACP activity peaked later and at a lower level (85.74 U/mL at 168 h; 26.10% of the total activity). NP and phytase also peaked later (95.75 U/mL and 16.36 U/mL on day 4, respectively). The shift towards ALP dominance is explained by the hydroxyapatite-like structure of PBC, which requires prior Ca^{2+}/Mg^{2+} dissociation to expose the phosphate groups for enzymatic hydrolysis, a step less critical for $Ca_3(PO_4)_2$. Additionally, ACP catalytic efficiency was inhibited by Mg^{2+} ions in PBC, which binded to the His159 residue at the active site[39].

Chelation of metal ions is a well-established chemical strategy for solubilizing insoluble phosphates. As demonstrated by synthetic chelators such as EDTA, the sequestration of ions such as Ca^{2+}, Fe^{3+}, and Al^{3+} disrupts the mineral lattice, causing phosphate to be released into the solution. The siderophores secreted by PSB1 are likely to sequester Fe^{3+} and Al^{3+} ions, thereby facilitating the dissolution of corresponding metal-bound phosphates (e.g., $FePO_4$, $AlPO_4$) and enhancing P

bioavailability. **Fig. 4f** shows the dynamic process of siderophore production in PSB1 as measured by Fe^{3+} release. Siderophore production was quantified using the CAS liquid assay, which is a standardized method for assessing siderophore activity based on Fe-chelating capacity. The assay relies on colorimetric changes that occur when siderophores competitively chelate Fe^{3+} from the CAS- Fe^{3+} complex, causing a decrease in absorbance at 465 nm. Siderophore production increased rapidly from trace amounts to 13.40 mg/L on day 1, peaked at 24.70 ± 2.10 mg/L on day 3, and declined to 15.50 ± 0.60 mg/L by day 7. This pattern closely resembled that of the bacterial growth curve. This initial surge in siderophore production was linked to the upregulation of siderophore biosynthesis genes (entC and foxA) under Fe-limited conditions. This decline corresponds to reduced bacterial growth and downregulation of the energy-intensive siderophore production pathway as Fe bioavailability increases through dissolution or cell lysis[40].

3.5 Analysis of P solubilization kinetics and release mechanism

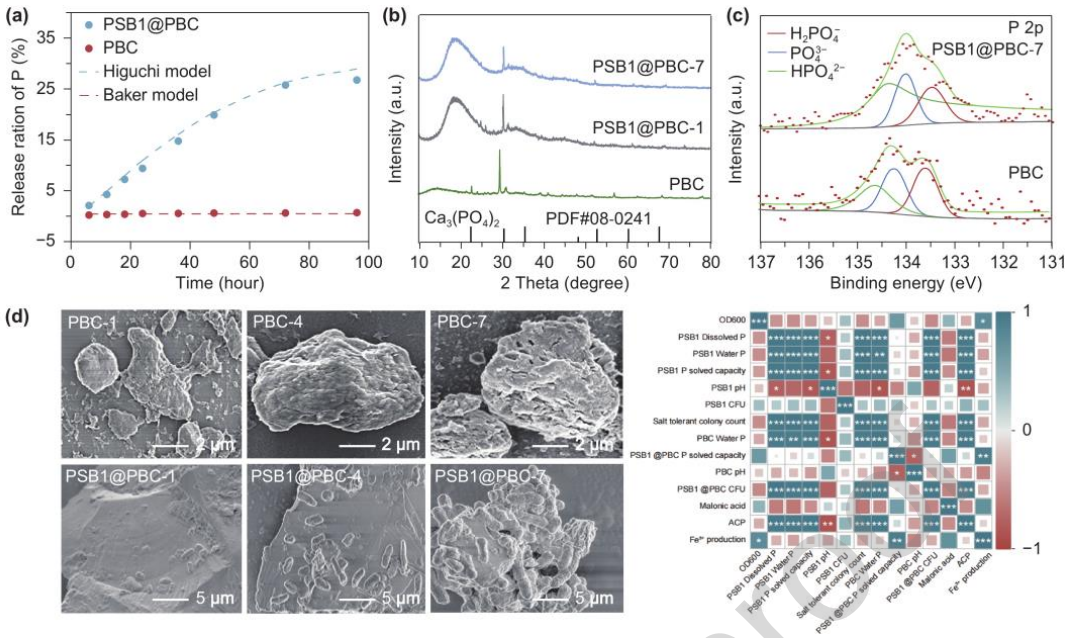

Fig. 5: Kinetics, characterization, and functional analysis of PSB1@PBC. a) P release rate kinetics of PSB1@PBC and PBC over time with curve fitting using the Higuchi and Baker models; b) XRD patterns of PBC (aqueous dissolution), PSB1@PBC-1(bacterially solubilized for 1 day), and PSB1@PBC-7 (bacterially solubilized for 7 days); c) XPS analysis of P in PBC (aqueous dissolution) and PSB1@PBC (bacterially solubilized for 7 day); d) SEM images of the aqueous dissolution state and bacterial dissolution state on days 1, 4, and 7; e) correlation heatmap analysis of PSB1@PBC system functionality.

Fig. 5a shows the P release kinetics of PBC and PSB1@PBC over 5 days. PBC released only 0.058 mg/g of P, whereas PSB1@PBC demonstrated a significantly higher cumulative release of 26.80 mg/g on day 4. To investigate the P release mechanisms, the first-order, Higuchi, Hixson–Crowell, Baker–Lonsdale, and Ritger–Peppas models were applied for curve fitting. The fitting parameters are listed in Table S2. The release of P from PBC was best described by the Baker–Lonsdale model ($R^2 = 0.994$), indicating a dissolution-controlled release[41]. This suggests that P release from PBC is limited by the slow dissolution of P through the microporous

structure of the biochar, which is consistent with the low solubility of mineral-bound P. In contrast, PSB1@PBC followed the Higuchi model (R^2 = 0.992), indicating diffusion-controlled release. Microbial activity, enzymatic catalysis, and chelation enhanced P solubilization and facilitated continuous diffusion through the modified biochar pores, explaining the sustained and improved P availability in PSB1@PBC[42].

To explore the structural changes related to P release, XRD analysis (**Fig. 5b**) was performed, which showed the crystallographic evolution of the PBC. The distinct diffraction peaks at 29.4° and 31.8° confirmed the presence of $Ca_3(PO_4)_2$. After 1 day in PSB1@PBC, the peaks decreased in intensity and broadened, indicating initial dissolution. By day 7, the crystallinity was significantly reduced, with a broad hump in the 20–25° range, indicating extensive amorphization due to microbial activity. The XPS analysis of the P 2p region (**Fig. 5c**) revealed that in PBC, P was mainly Ca-bound, with a peak at 134.2 eV. After 7 days in PSB1@PBC, the spectrum split into two peaks: a mineral P peak at 134.2 eV and a new peak at 133.7 eV, indicating bioavailable forms such as $H_2PO_4^-$ or $NaHCO_3^-$ extractable P. This shows the microbial conversion of mineral P into labile plant-available forms without significant TP loss. The SEM images (**Fig. 5d**) show structural changes at the biochar-microbe interface. In the control group (PBC in LB broth), the PBC structure remained unchanged with no microbial colonization and only minor inorganic deposits by day 7. In contrast, PSB1@PBC exhibited time-dependent microbial colonization. Sparse

bacterial cells adhered to pore edges on day 1. By day 4, bacterial proliferation and microcolony formation enhanced the local acid and enzyme concentrations. By day 7, a continuous biofilm developed, which facilitated metabolite exchange and retained solubilized P, thereby supporting sustained and efficient P release from PSB1@PBC.

The heatmap in **Fig. 5e** shows the Pearson correlation coefficients of the 12 variables affecting P solubilization in the PSB1@PBC system. Strong positive correlations ($r = 0.7$, $p < 0.001$) are red, whereas negative correlations ($r = -0.6$) are blue. Salt-tolerant colony counts were strongly correlated with PSB1@PBC CFU ($r = 0.89$, $p < 0.001$) and free PSB1 CFU ($r = 0.76$, $p < 0.01$), confirming that PBC protects bacteria from osmotic stress, which is consistent with the SEM observations (**Fig. 3c**). Cell densities negatively correlated with PBC pH ($r = -0.71$ and $r = -0.68$, respectively, $p < 0.01$), reflecting acidification-driven growth. The pH dropped from 6.0 to 3.9 within 96 h (**Fig. 3d**) as a result of malonic acid secretion, which dissociated 62% of the Ca^{2+} from the PBC hydroxyapatite. Malonic acid was most strongly correlated with PSB1@PBC P solubility ($r = 0.93$, $p < 0.001$), surpassing free PSB1 ($r = 0.81$, $p < 0.001$), owing to bidentate Ca^{2+} chelation ($K = 10^{6.5}$), which reduced the lattice energy by 23%. Its negative correlation with pH ($r = -0.85$, $p < 0.001$) confirmed proton-mediated dissolution. At pH 4.5, 78% dissociation enabled continuous Ca–P cleavage. ACP activity was positively correlated with Fe^{3+} ($r = 0.79$, $p < 0.001$), indicating synergistic metal chelation and hydrolysis. Fe^{3+}-siderophore complexes ($K = 10^{20.5}$) solubilized $FePO_4$, releasing PO_4^{3-} for ACP mineralization (**Fig. 4f**). ACP inversely

correlated with PBC water P ($r = -0.63$, $p < 0.05$), suggesting microbial reuptake of solubilized P. PSB1@PBC P solubility correlated more with Fe carriers ($r = 0.72$, $p < 0.001$) than free PSB1 ($r = 0.51$, $p < 0.01$), reflecting PBC-enhanced Fe^{3+} reduction. XPS revealed a 2.1-fold increase in the Fe^{2+}/Fe^{3+} ratio in PSB1@PBC. The minimal correlation between PBC water P and microbes indicated 31% readsorption by PBC, suggesting that acid-overproducing strains could outcompete biochar for P binding[43].

3.6 Integrated multi-pathway mechanisms for P solubilization

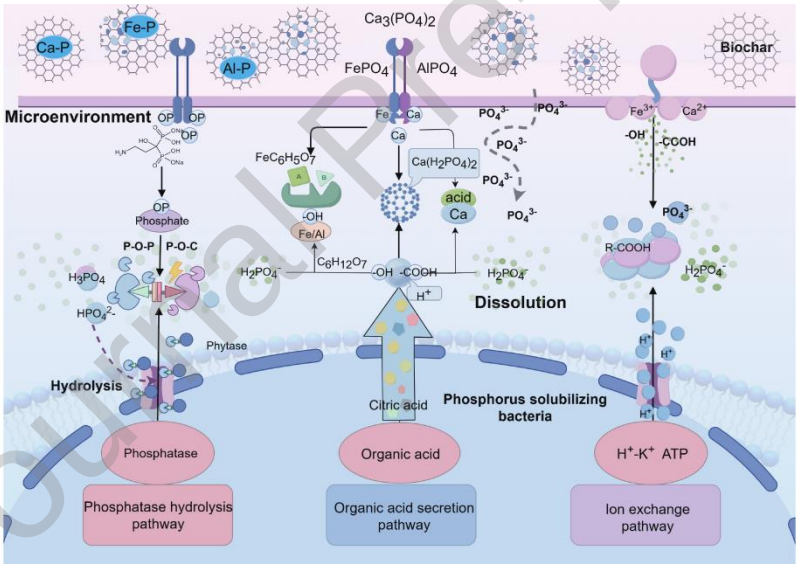

Fig. 6: Three mechanistic pathways for PSB1 to dissolve insoluble P in PBC.

We clarified the multifaceted strategies and mechanisms through which PSB1@PBC enhances P bioavailability by drawing on the experimental results (**Fig. 6**). In the organic acid-driven pathway, PSB1 secreted low-molecular-weight acids, including malonic, α-ketoglutaric, and butyric acids (**Fig. 4a**). These acids released protons that acidified the microenvironment, thereby promoting the dissolution of mineral

phosphates according to the reaction: $Ca_5(PO_4)_3OH + 7H^+ \rightarrow 5Ca^{2+} + 3H_2PO_4^- + H_2O$. Additionally, the anions of these organic acids chelated metal cations (e.g., Fe^{3+} and Al^{3+}), forming soluble complexes that displaced phosphate (e.g., $FePO_4 + C_6H_5O_7^{3-} \rightarrow FeC_6H_5O_7 + PO_4^{3-}$). This process generated bioavailable forms of P, specifically $H_2PO_4^-$ and HPO_4^{2-}. Experimental data on acid secretion dynamics (**Fig. 4a–c**) support this mechanism and are consistent with previous studies on organic acid-mediated phosphate dissolution[15]. In the enzymatic hydrolysis pathway, microbial phosphatases and phytases acted on organic and mineral-bound P by cleaving P-O-C and P-O-P bonds in compounds such as phytates (**Figs. 4d and 4e**). These enzymes demonstrated high catalytic efficiency, with optimal activity observed at 37 °C (31.75 ± 3.1 U/mL, **Fig. S9a–b**). The PBC matrix enhanced this enzymatic process by concentrating enzymes and substrates on its surface, thereby facilitating the formation of orthophosphate (H_3PO_4). This pathway is consistent with the established mechanisms of enzymatic dephosphorylation reported for PSB[44]. In the ion-exchange pathway, H^+-ATPase activity generated a proton-rich zone at the cell-biochar interface **(Fig. 3e**), which promoted cation exchange with phosphate-bound metals (e.g., $Ca_3(PO_4)_2 + 4H^+ \rightarrow 2H_2PO_4^- + 3Ca^{2+}$). PBC facilitated this exchange through its ion-binding surface functional groups (-COOH, -OH), further enhancing phosphate mobilization[45]. Acidolysis, chelation, enzymatic dephosphorylation, and proton-coupled exchange processes operate synergistically within the PSB1@PBC composite, effectively converting insoluble P into plant-available forms.

4. Conclusion

In this study, a highly efficient, stress-tolerant, phosphate-solubilizing bacterium, *R. ornithinolytica* (PSB1), was isolated from SS and immobilized on PBC to create a composite PSB1@PBC. Compared to unmodified PBC, the release of soluble P from this composite increased 17.5-fold, reaching 26.80 mg/g within 4 days. P release was driven by three synergistic mechanisms: i) malonic acid-induced acidification (Ca^{2+}/Mg^{2+} ion chelation), ii) enzymatic mineralization by ALP, and iii) siderophore-mediated chelation, promoting mineral dissolution. Hedley extraction confirmed the conversion of stable HCl-P to bioavailable $NaHCO_3$-P with minimal TP loss. Kinetic analysis (Higuchi model, $R^2 = 0.992$) revealed a diffusion-controlled, sustained release of P. The formation of a biofilm on biochar enhanced long-term microbial-mineral interactions. This study demonstrates the potential of biochar-based biocomposites to improve nutrient cycling and agricultural sustainability, and close the global P loop.

Declaration of Competing Interest

The authors declare that they have no known competing financial interests or personal relationships that could have appeared to influence the work reported in this paper.

Acknowledgements

This work was supported by the Science and Technology Program–Regional Innovation Guidance Program (2023ZD080), Science and Technology Planning

Project (2024DA052), Tianchi Talent Project (CZ002735(3123), BT2025TCYC0060), National Natural Science Foundation (22408237, 32541085), Research Initiation Project of Shihezi University (RCZK202330), Science and Technology Group of Xi'an Polytechnic University Assists the Urumqi Project, and Science and Higher Education of the Russian Federation (1240122001838).

References

[1] T. Qian, W.S. Ong, D. Lu, Y. Zhou, A potential phosphorus fertilizer to alleviate the coming “phosphorus crisis”-biochar derived from enhanced biological phosphorus removal sludge, Science of The Total Environment 838 (2022) 156559.

[2] S. Ghysels, D. Rathnayake, P. Maziarka, O. Mašek, S. Sohi, F. Ronsse, Biochar stability scores from analytical pyrolysis (Py-GC-MS), Journal of Analytical and Applied Pyrolysis 161 (2022) 105412.

[3] J. Li, Y. Wu, D. Li, P. Tang, W. Zhang, Q. Zhao, W. Guo, Y. Zhu, Y. Peng, Combined effect of thermal hydrolysis process and low-temperature pyrolysis on the classification and bioavailability of phosphorus in sewage sludge, Bioresource Technology 407 (2024) 131135.

[4] J. Liu, N. Zhu, Y. Zhang, T. Ren, C. Shao, R. Shi, X. Li, M. Ju, T. Ma, Q. Yu, Transcription profiling-guided remodeling of sulfur metabolism in synthetic bacteria for efficiently capturing heavy metals, Journal of Hazardous Materials 403 (2021) 123638.

[5] X. Li, S. Lin, T. Hao, S.K. Khanal, G. Chen, Elucidating pyrolysis behaviour of activated sludge in granular and flocculent form: Reaction kinetics and mechanism, Water Research 162 (2019) 409–419.

[6] T. Wang, Y. Zhai, Y. Zhu, C. Peng, T. Wang, B. Xu, C. Li, G. Zeng, Feedwater pH affects phosphorus transformation during hydrothermal carbonization of sewage sludge, Bioresource Technology 245 (2017) 182–187.

[7] J. Liu, A.P. Davis, Phosphorus Speciation and Treatment Using Enhanced Phosphorus Removal Bioretention, Environ. Sci. Technol. 48 (2014) 607–614.

[8] T. Qian, Q. Yang, D.C.F. Jun, F. Dong, Y. Zhou, Transformation of phosphorus in sewage sludge biochar mediated by a phosphate-solubilizing microorganism, Chemical Engineering Journal 359 (2019) 1573–1580.

[9] A.E. Ortega-Torres, E. Rico-García, R. Guzmán-Cruz, I. Torres-Pacheco, E.G. Tovar-Pérez, R.G. Guevara-González, Addition of Phosphatases and Phytases to Mature Compost to Increase Available Phosphorus: A Short Study, Agronomy 11

(2021) 2555.

[10]Y. Zhou, X. Zhao, Y. Jiang, C. Ding, J. Liu, C. Zhu, Synergistic remediation of lead pollution by biochar combined with phosphate solubilizing bacteria, Science of The Total Environment 861 (2023) 160649.

[11]M. Gao, N. Yang, Y. Shao, T. Shen, W. Li, B. Ma, X. Wei, Y.-L. Ruan, F. Ma, M. Li, An insertion in the promoter of a malate dehydrogenase gene regulates malic acid content in apple fruit, Plant Physiology 196 (2024) 432–445.

[12]S. Wang, M. Song, C. Wang, X. Dou, X. Wang, X. Li, Mechanisms underlying soil microbial regulation of available phosphorus in a temperate forest exposed to long-term nitrogen addition, Science of The Total Environment 904 (2023) 166403.

[13]Z. Yang, Z. Liu, F. Zhao, L. Yu, W. Yang, M. Si, Q. Liao, Organic acid, phosphate, sulfate and ammonium co-metabolism releasing insoluble phosphate by Klebsiella aerogenes to simultaneously stabilize lead and cadmium, Journal of Hazardous Materials 443 (2023) 130378.

[14]L. Liu, Y.-P. Yang, G.-L. Duan, J. Wang, X.-J. Tang, Y.-G. Zhu, The chemical-microbial release and transformation of arsenic induced by citric acid in paddy soil, Journal of Hazardous Materials 421 (2022) 126731.

[15]D. Menezes-Blackburn, C. Paredes, H. Zhang, C.D. Giles, T. Darch, M. Stutter, T.S. George, C. Shand, D. Lumsdon, P. Cooper, R. Wendler, L. Brown, M. Blackwell, C. Wearing, P.M. Haygarth, Organic Acids Regulation of Chemical–Microbial Phosphorus Transformations in Soils, Environ. Sci. Technol. 50 (2016) 11521–11531.

[16]L.-Y. Yu, H.-B. Huang, X.-H. Wang, S. Li, N.-X. Feng, H.-M. Zhao, X.-P. Huang, Y.-W. Li, H. Li, Q.-Y. Cai, C.-H. Mo, Novel phosphate-solubilising bacteria isolated from sewage sludge and the mechanism of phosphate solubilisation, Science of The Total Environment 658 (2019) 474–484.

[17]B. Sashidhar, A. r. Podile, Mineral phosphate solubilization by rhizosphere bacteria and scope for manipulation of the direct oxidation pathway involving glucose dehydrogenase, Journal of Applied Microbiology 109 (2010) 1–12.

[18]Y. Tang, C. Wang, P.E. Holm, H.Chr.B. Hansen, K.K. Brandt, Impacts of biochar

materials on copper speciation, bioavailability, and toxicity in chromated copper arsenate polluted soil, Journal of Hazardous Materials 459 (2023) 132067.

[19] Y. Fu, M. Jia, F. Wang, Z. Wang, Z. Mei, Y. Bian, X. Jiang, M. Virta, J.M. Tiedje, Strategy for Mitigating Antibiotic Resistance by Biochar and Hyperaccumulators in Cadmium and Oxytetracycline Co-contaminated Soil, Environ. Sci. Technol. 55 (2021) 16369 – 16378.

[20] C. Wang, G. Wang, S. Xie, Z. Dong, L. Zhang, Z. Zhang, J. Song, Y. Deng, Phosphorus-rich biochar modified with Alcaligenes faecalis to promote U(VI) removal from wastewater: Interfacial adsorption behavior and mechanism, Journal of Hazardous Materials 454 (2023) 131484.

[21] J. Li, Y. Li, F. Liu, X. Zhang, M. Song, R. Li, Pyrolysis of sewage sludge to biochar: Transformation mechanism of phosphorus, Journal of Analytical and Applied Pyrolysis 173 (2023) 106065.

[22] A. Raj, A. Yadav, S. Arya, R. Sirohi, S. Kumar, A.P. Rawat, R.S. Thakur, D.K. Patel, L. Bahadur, A. Pandey, Preparation, characterization and agri applications of biochar produced by pyrolysis of sewage sludge at different temperatures, Science of The Total Environment 795 (2021) 148722.

[23] B. Xiao, Q. Dai, X. Yu, P. Yu, S. Zhai, R. Liu, X. Guo, J. Liu, H. Chen, Effects of sludge thermal-alkaline pretreatment on cationic red X-GRL adsorption onto pyrolysis biochar of sewage sludge, Journal of Hazardous Materials 343 (2018) 347–355.

[24] A.A. Karim, M. Kumar, S. Mohapatra, S.K. Singh, Nutrient rich biomass and effluent sludge wastes co-utilization for production of biochar fertilizer through different thermal treatments, Journal of Cleaner Production 228 (2019) 570–579.

[25] Z. Wang, B. Chen, Y. Cao, S. Xing, B. Zhang, S. Wang, H. Tian, Insights into the interfacial dynamics and interaction mechanisms between phosphate-solubilizing bacteria and straw-derived biochar, Biochar 7 (2025) 55.

[26] T. Qian, D. Lu, Y.N.A. Soh, R.D. Webster, Y. Zhou, Biotransformation of phosphorus in enhanced biological phosphorus removal sludge biochar, Water Research 169 (2020) 115255.

[27]M. Song, X. Wang, H. Xu, X. Zhou, C. Mu, Effect of Trichoderma viride on insoluble phosphorus absorption ability and growth of Melilotus officinalis, Sci Rep 13 (2023) 12345.

[28]F. Yang, S. Zhang, J. Song, Q. Du, G. Li, N.V. Tarakina, M. Antonietti, Synthetic Humic Acids Solubilize Otherwise Insoluble Phosphates to Improve Soil Fertility, Angewandte Chemie International Edition 58 (2019) 18813–18816.

[29]J.-L. Liang, J. Liu, P. Jia, T. Yang, Q. Zeng, S. Zhang, B. Liao, W. Shu, J. Li, Novel phosphate-solubilizing bacteria enhance soil phosphorus cycling following ecological restoration of land degraded by mining, The ISME Journal 14 (2020) 1600–1613.

[30]H.-L. Zhang, G.-P. Sheng, W. Fang, Y.-P. Wang, C.-Y. Fang, L.-M. Shao, H.-Q. Yu, Calcium effect on the metabolic pathway of phosphorus accumulating organisms in enhanced biological phosphorus removal systems, Water Research 84 (2015) 171–180.

[31]F. Wang, S. Ma, X. Han, S. Liu, K. Sun, Enhancing Phosphorus Release from Sewage Sludge in Anaerobic Digestion via Thermal Hydrolysis Pretreatment: Insights from Phosphorus Speciation and Molecular Biological Pathways, Environ. Sci. Technol. 58 (2024) 10828–10838.

[32]J.K. Guo, Y.Z. Ding, R.W. Feng, R.G. Wang, Y.M. Xu, C. Chen, X.L. Wei, W.M. Chen, Burkholderia metalliresistens sp. nov., a multiple metal-resistant and phosphate-solubilising species isolated from heavy metal-polluted soil in Southeast China, Antonie van Leeuwenhoek 107 (2015) 1591–1598.

[33]X. Zhu, W. Gong, W. Li, C. Zhang, Fixating lead in coal gangue with phosphate using phosphate-dissolving bacteria: Phosphorus dissolving characteristics of bacteria and adsorption mechanism of extracellular polymer, Journal of Hazardous Materials 458 (2023) 131923.

[34]H. Wang, K. Xiao, J. Yang, Z. Yu, W. Yu, Q. Xu, Q. Wu, S. Liang, J. Hu, H. Hou, B. Liu, Phosphorus recovery from the liquid phase of anaerobic digestate using biochar derived from iron−rich sludge: A potential phosphorus fertilizer, Water

Research 174 (2020) 115629.

[35]W. Sun, Y. Li, L.R. McGuinness, S. Luo, W. Huang, L.J. Kerkhof, E.E. Mack, M.M. Häggblom, D.E. Fennell, Identification of Anaerobic Aniline-Degrading Bacteria at a Contaminated Industrial Site, Environ. Sci. Technol. 49 (2015) 11079–11088.

[36]L. Lu, W. Qin, M. Wu, Q. Chen, B. Pan, B. Xing, Biochar promotes FePO4 solubilization through modulating organic acids excreted by Talaromyces pinophilus, Carbon Res. 4 (2025) 27.

[37]G. Zhao, Y. Sheng, C. Li, Q. Liu, N. Hu, Restraint of enzymolysis and photolysis of organic phosphorus and pyrophosphate using synthetic zeolite with humic acid and lanthanum, Chemical Engineering Journal 386 (2020) 123791.

[38]H. Chen, F. Min, X. Hu, D. Ma, Z. Huo, Biochar assists phosphate solubilizing bacteria to resist combined Pb and Cd stress by promoting acid secretion and extracellular electron transfer, Journal of Hazardous Materials 452 (2023) 131176.

[39]J.H. Park, N. Bolan, M. Megharaj, R. Naidu, Isolation of phosphate solubilizing bacteria and their potential for lead immobilization in soil, Journal of Hazardous Materials 185 (2011) 829–836.

[40]M. Chen, Y. Huang, Y. Wang, C. Liu, Y. He, N. Li, Inhibitory effects and mechanisms of insoluble humic acids on internal phosphorus release from the sediments, Water Research 250 (2024) 121074.

[41]L. Wang, H. Zhang, Y. Zhang, Y. Song, 13C metabolic flux analysis on roles of malate transporter in lipid accumulation of Mucor circinelloides, Microbial Cell Factories 18 (2019) 154.

[42]Q. Liu, K. Meki, H. Zheng, Y. Yuan, M. Shao, X. Luo, X. Li, Z. Jiang, F. Li, B. Xing, Biochar application in remediating salt-affected soil to achieve carbon neutrality and abate climate change, Biochar 5 (2023) 45.

[43]L. Pan, B. Cai, Phosphate-Solubilizing Bacteria: Advances in Their Physiology, Molecular Mechanisms and Microbial Community Effects, Microorganisms 11 (2023) 2904.

[44]Y. Jiang, C. Ren, H. Guo, M. Guo, W. Li, Speciation Transformation of Phosphorus in Poultry Litter during Pyrolysis: Insights from X-ray Diffraction, Fourier Transform Infrared, and Solid-State NMR Spectroscopy, Environ. Sci. Technol. 53 (2019) 13841–13849.

[45]N. Edayilam, D. Montgomery, B. Ferguson, A.S. Maroli, N. Martinez, B.A. Powell, N. Tharayil, Phosphorus Stress-Induced Changes in Plant Root Exudation Could Potentially Facilitate Uranium Mobilization from Stable Mineral Forms, Environ. Sci. Technol. 52 (2018) 7652–7662.

Declaration of interests

The authors declare that they have no known competing financial interests or personal relationships that could have appeared to influence the work reported in this paper.

Highlights:

1.A novel biochar-microbe composite for enhanced phosphorus release.

2. Superior bacterial phosphate solubilization under saline-alkaline stress.

3. Multi-mechanism P solubilization via malonic acid, phosphatase and siderophores.

4. Converts mineral-bound P to a bioavailable form without P loss.

5. Sustained P release kinetics with high agricultural potential.